Dependence of superintensity of tropical cyclones on SST in axisymmetric numerical simulations

Yuanlong Li[1,2], Yuqing Wang[2,3*], Yanluan Lin[1], Rong Fei[3,2]

[1]Ministry of Education Key Laboratory for Earth System Modeling, Department of Earth System Science, and Joint Center for Global Change Studies (JCGCS), Tsinghua University, Beijing, China.

[2]International Pacific Research Center and Department of Atmospheric Sciences, School of Ocean and Earth Science and Technology, University of Hawaii at Mānoa, Honolulu, Hawaii, USA.

[3]State Key Laboratory of Severe Weather, Chinese Academy of Meteorological Sciences, China Meteorological Administration, Beijing, China.

May 2, 2020 (submitted)

July 10, 2020 (first revision)

September 20, 2020 (second revision)

Dateline

Submitted to ***Monthly Weather Review***

[*]Corresponding author address:
Prof. Yuqing Wang
International Pacific Research Center
University of Hawaii at Manoa
404A/POST, 1680 East West Road,
Honolulu, HI 96822, USA.
Email: yuqing@hawaii.edu

Abstract

This study revisits the superintensity of tropical cyclones (TCs), which is defined as the excess maximum surface wind speed normalized by the corresponding theoretical maximum potential intensity (MPI), based on ensemble axisymmetric numerical simulations, with the focus on the dependence of superintensity on the prescribed sea surface temperature (SST) and the initial environmental atmospheric sounding. Results show a robust decrease of superintensity with increasing SST no matter in experiments with an SST-independent initial atmospheric sounding or in those with the SST-dependent initial atmospheric soundings as in nature sorted for the western North Pacific and the North Atlantic. It is found that the increase in either convective activity (and thus diabatic heating) in the TC outer region or theoretical MPI or both with increasing SST could reduce the superintensity. For a given SST-independent initial atmospheric sounding, the strength of convective activity in the TC outer region increases rapidly with increasing SST due to the rapidly increasing air-sea thermodynamic disequilibrium (and thus potential convective instability) with increasing SST. As a result, the decrease of superintensity with increasing SST in the SST-independent sounding experiments is dominated by the increasing convective activity in the TC outer region and is much larger than that in the SST-dependent sounding experiments, and the TC intensity becomes sub-MPI at relatively high SSTs in the former. Due to the marginal increasing tendency of convective activity in the TC outer region, the decrease of superintensity in the latter is dominated by the increase in theoretical MPI with increasing SST.

1. Introduction

To accurately estimate the upper bound of the intensity of a tropical cyclone (TC) is important for TC risk assessment and management in both weather and climate time scales. Such an upper bound of the intensity that a TC can reach under favorable environmental thermodynamic conditions is termed the maximum potential intensity (MPI). Over the past decades, different approaches have been used to estimate the TC MPI, such as the sea surface temperature (SST) based statistical analysis (e.g., DeMaria and Kaplan 1994; Whitney and Hobgood 1997) and the direct analytical derivations (e.g., Emanuel 1986, 1995, 1997; Holland 1997; Bister and Emanuel 1998; Rousseau-Rizzi and Emanuel 2019). Because its physically based nature and low computational cost and good performance (e.g., Emanuel 2000), the theoretical MPI proposed by Emanuel (1986, 1997) has been widely used to study both weather and climate aspects of TCs.

The Emanuel's MPI theory conceptualizes a mature TC as a Carnot heat engine (Emanuel 1986, 1997). There are two versions of the Emanuel's theoretical MPI. The earlier version assumes gradient wind and thermal wind balances and gives the steady-state maximum gradient wind speed at the top of the boundary layer (e.g., Emanuel 1986, 1995). The latest version is based on the energy cycle of a Carnot heat engine and provides the steady-state maximum surface total wind speed (Emanuel 1997; Bister and Emanuel 1998; Rousseau-Rizzi and Emanuel 2019). Compared with the earlier gradient-wind-based MPI, the latest surface-wind-based MPI is obtained with less assumptions/approximations and is also more practical because the TC intensity is commonly defined as the maximum near-surface total wind speed (Rousseau-Rizzi and Emanuel 2019). There are two different, but related, derivations of the surface-wind-based MPI (Emanuel 1997; Rousseau-Rizzi and Emanuel 2019). Although the derivation in Rousseau-Rizzi and Emanuel (2019) is under debate (Montgomery and Smith 2020; Rousseau-Rizzi and Emanuel 2020), the two derivations (Emanuel 1997; Rousseau-Rizzi and Emanuel 2019) yield the same mathematical formula for the MPI. In both derivations, the theoretical MPI can be yielded from a balance between the surface available power production and power dissipation near the radius of maximum wind (RMW) and can be expressed in terms of the maximum surface total wind speed ($|\boldsymbol{V}_{MPI}|$) as given below.

$$|\boldsymbol{V}_{MPI}| = \sqrt{\frac{C_k}{C_D}\epsilon T_s(s_0^* - s_b)|_{\mathrm{RMW}}}, \tag{1}$$

where C_k and C_D are the sea surface exchange coefficients of enthalpy and momentum, respectively, T_s is the SST, s_0^* is the saturation entropy at the SST, s_b is the near-surface entropy, and ϵ is the thermodynamic efficiency, defined as $(T_s - T_o)/T_s$ (T_o is the mean air temperature of the TC's outflow). All variables in Eq. (1) are regarded as those in the steady state of a TC. Note that the denominator T_s of ϵ would be replaced by T_0 if the dissipative heating is considered (Bister and Emanuel 1998). In this study, the surface-wind-based MPI will be used as the theoretical MPI.

Although the Emanuel's MPI theory has been shown to be able to reasonably estimate TC maximum intensity (e.g., Emanuel 2000; Bister and Emanuel 2002), some observational and numerical studies found that the intensity of TCs may exceed the corresponding MPI (e.g., Tonkin 2000; Hausman 2001; Persing and Montgomery 2003; Montgomery et al. 2006; Bryan and Rotunno 2009a,b; Wang and Xu 2010). Such a phenomenon was called superintensity by Persing and Montgomery (2003), who hypothesized that the low-level high entropy air entrained from the eye into the eyewall, which is omitted in the Emanuel's MPI theory, can be an extra energy source to fuel the TC heat engine. However, using an axisymmetric TC model, Bryan and Rotunno (2009a) demonstrated that the contribution of the high entropy air in the low-level eye to the maximum intensity of the simulated TC was less than 4% and thus should not be significant. In a follow-up study, Wang and Xu (2010) proposed that the superintensity (mainly for the surface-wind-based MPI) was dominantly contributed by the inward transport of power production outside the RMW. They found that in the steady-state stage of the simulated TC, the available power production could not balance the power dissipation due to surface friction under the eyewall (near the RMW). They showed that in addition to the primary power production under the eyewall, the power production outside the eyewall up to about 2–2.5 times of the RMW was needed to balance the power dissipation under the eyewall. Some studies have attributed superintensity (mainly for the gradient-wind-based MPI) to the unbalanced flow or the supergradient wind in TC boundary layer (Bryan and Rotunno 2009b; Frisius et al. 2013).

In a recent study, Rousseau-Rizzi and Emanuel (2019) evaluated the TC superintensity, with the focus on the surface-wind-based MPI, in axisymmetric models. They defined the superintensity as the normalized excess of maximum surface wind speed of the simulated TC relative to the theoretical MPI. By varying the parameterized turbulent horizontal mixing length in axisymmetric simulations, Rousseau-Rizzi and Emanuel (2019) found that the superintensity only exists in those simulations with weak horizontal mixing (as the mixing length lower than ~500 m) and converges to a state with a marginal superintensity of ~5% in the inviscid limit as assumed in the MPI theory. They showed that the simulated TC intensity is weaker than the theoretical MPI (sub-MPI) in simulations with strong mixing and becomes weakly superintense with weak mixing. This is in sharp contrast to ~50% superintensity reported in Persing and Montgomery (2003) and Wang and Xu (2010). Some other studies have shown that the maximum intensity (and superintensity) of numerically simulated TCs can be very sensitive to parameterizations of other subgrid-scale processes as well (Bryan and Rotunno 2009b; Bryan 2012; Rousseau-Rizzi and Emanuel 2019).

We notice that most of previous studies on the superintensity have been based on simulations with a given SST and a certain initial environmental atmospheric sounding. For example, using the same moist tropical atmospheric sounding of Dunion (2011), the SST was fixed to be 29ºC in Bryan (2012), 28ºC in Peng et al. (2018), and 27ºC in Tao et al. (2019). With the modified Jordan (1958)'s mean tropical atmospheric sounding of Rotunno and Emanuel (1987), which was neutral to convection at the initial time, the SST was set at 26.13ºC in Persing and Montgomery (2003) and 27ºC in Rousseau-Rizzi and Emanuel (2019). Note that for a given environmental atmospheric sounding (even initially neutral), a higher SST implies a higher surface heat exchange and thus a faster production rate of convective available potential energy (CAPE) or convective instability after the model integration (Emanuel 1994), and thus a condition more favorable for the development of convection in the TC environment (e.g., Sun et al. 2017). Although strong convection in the inner core can maintain and enhance TC intensity, the convective activity in the outer region could be detrimental to TC intensity (Bister 2001; Wang 2009; Xu and Wang 2010). This suggests that the superintensity may vary with SST under a given environmental atmospheric sounding. Therefore, different degrees of superintensity among previous studies could be partly attributed to the use of different combinations of SST and environmental atmospheric sounding. However, this possible dependence has not been studied in the literature. Furthermore, it is unclear whether the TC superintensity may depend on SST in nature or vary with the initial atmospheric sounding.

In this study, two sets of ensemble numerical experiments were performed to address the above issues. In one set, experiments were conducted with different SSTs and the SST-independent initial atmospheric sounding of Dunion (2011). In the other set, experiments were conducted with different SSTs but using the SST-dependent atmospheric soundings obtained from observations over the North Atlantic and the western North Pacific, respectively. In both sets, additional sensitivity experiments with varying surface drag coefficient together with SST were also performed to examine the effect of change in theoretical MPI with SST on the dependence of superintensity on SST. We will show that a non-negligible superintensity appears when the power dissipation is larger than the available power production locally under the eyewall, consistent with the definition of superintensity in the current surface-wind-based MPI framework. However, the superintensity only occurs at relatively low SSTs but becomes sub-MPI at relatively high SSTs in the SST-independent initial sounding experiments. A new result is the decrease of superintensity with increasing SST because of the increase in either convective activity in the TC outer region or theoretical MPI or both as SST increases. The detailed model settings and experimental design are described in Section 2. Main results are presented in Sections 3 and 4, respectively, for SST-independent and SST-dependent initial atmospheric soundings. Conclusions and implications of the results are summarized and discussed in the last section.

2. Model and experimental design

The model used was the state-of-the-art axisymmetric cloud model (CM1), version 19.8 (Bryan and Fritsch 2002). The model domain had dimensions 3100 km × 25 km in radial and vertical directions, respectively. The radial grid spacing within 100-km radius was 1 km and was stretched to 12 km at the outer boundary. The model atmosphere had 59 levels in the vertical with stretched grids below 5.5 km as in Li et al. (2019). An f-plane was assumed with the Coriolis parameter of 5×10^{-5} s^{-1}. The double-moment microphysics scheme of Thompson et al. (2008) was used for cloud/precipitation processes, and no cumulus convective parameterization was used in all simulations. Newtonian cooling, capped at 2 K d^{-1}, was added to the perturbation potential temperature equation to mimic radiative cooling (Rotunno and Emanuel 1987), and dissipative heating was not considered in this study. The subgrid-scale turbulent mixing was parameterized using the Smagorinsky scheme (Bryan and Fritsch 2002), with the horizontal and asymptotic vertical mixing lengths being fixed at 700 m (Zhang and Montgomery 2012) and 70 m (Zhang and

Drennan 2012), respectively. A constant exchange coefficient of 1.2×10^{-3} was used for surface enthalpy flux calculation, while the wind-dependent surface drag coefficient of Donelan et al. (2004) was used for surface stress calculation as

$$C_D = \begin{cases} C_{D0}\,, & |\boldsymbol{V}| \le 5\ \mathrm{m\ s^{-1}} \\ C_{D0} + (C_{D1} - C_{D0})(|\boldsymbol{V}| - 5)/20\,, & 5\ \mathrm{m\ s^{-1}} < |\boldsymbol{V}| \le 25\ \mathrm{m\ s^{-1}}, \\ C_{D1}\,, & 25\ \mathrm{m\ s^{-1}} < |\boldsymbol{V}| \end{cases} \quad (2)$$

where $|\boldsymbol{V}|$ is the surface total wind speed and C_{D0} and C_{D1} denote the lower and upper limits of surface drag coefficient, set to 1.0×10^{-3} and 2.4×10^{-3} as the default, respectively.

To examine the possible dependence of superintensity on SST, two sets of experiments were conducted in this study. In the first set of experiments, the moist tropical sounding of Dunion (2011) was used as the unperturbed environmental atmospheric sounding, which corresponds to the surface air temperature of ~26.8ºC with an environmental CAPE of ~2000 J Kg^{-1}. In this set, six experiments with all default setting as described above were first performed with SSTs varying from 27 to 32ºC at 1ºC interval, labeled as SST27–SST32. Note that with the SST-independent initial atmospheric sounding, the air-sea thermodynamic disequilibrium and thus surface enthalpy flux would increase rapidly with increasing SST. As a result, the production rates of CAPE and convective instability in the TC environment would increase, facilitating more active convective activity in the TC outer region. As we will discuss in Sections 3 and 4, in the SST-independent atmospheric sounding experiments with relatively high SSTs, active convection developed in the TC outer region because of the high air-sea thermodynamic disequilibrium, which is detrimental to the simulated steady-state intensity but has a marginal effect on the theoretical MPI, and thus the superintensity would be reduced. On the other hand, considering that the theoretical MPI, namely the denominator of the defined superintensity, would also increase with increasing SST (Eq. 1), the dependence of superintensity on SST may be affected by change in theoretical MPI.

Because $|\boldsymbol{V}_{MPI}| \propto \sqrt{C_k/C_D}$ (Eq. 1) in the steady state, one method to reduce the dependence of theoretical MPI on SST is to vary either C_k or C_D (namely C_{D1} as the surface wind speed greater than 25 m s^{-1}; Eq. 2) together with SST. However, changing C_k would also change the air-sea thermodynamic disequilibrium. Therefore, to examine the effect of change in theoretical MPI on the dependence of superintensity on SST, five additional sensitivity experiments as SST28–SST32 but using different C_{D1} from SST27 or the default ($C_{D1,27}$=2.4×10^{-3}) were performed, with the C_{D1} in each SST sensitivity experiment (i) determined by

$$C_{D1,i} = \left(\frac{|V_{MPI}|_i}{|V_{MPI}|_{27}}\right)^2 C_{D1,27}, \qquad (3)$$

where $|V_{MPI}|_i$ and $|V_{MPI}|_{27}$ denote the theoretical MPI under the default C_{D1} (2.4×10^{-3}). In this way, the new theoretical MPI in each sensitivity experiment would be similar to that in SST27. The results (Section 3) further confirm that the increasing convective activity in the TC outer region with increasing SST dominates the decrease of superintensity in the SST-independent atmospheric sounding experiments.

In the second set of experiments, the realistic SST-dependent atmospheric sounding was used for a given SST. The initial unperturbed environmental atmospheric sounding for each SST was constructed based on the monthly mean European Centre for Medium-Range Weather Forecasts (ECMWF) Interim reanalysis data (ERA-Interim, Dee et al 2011). Specifically, the vertical profiles of air temperature and specific humidity and sea level pressure (SLP) in a given region were sorted for each of SST bins of 1ºC interval (e.g., the bin for SST of 27ºC ranges between 26.5 and 27.5ºC, and so on) during June–November based on the $1^{\mathrm{o}} \times 1^{\mathrm{o}}$ gridded ERA-Interim data during 2009–2018. Two regions with active TC activities were chosen, one was the western North Pacific (WNP, 5ºN–20ºN, 130ºE–160ºE) and the other was the North Atlantic (NA, 5ºN–20ºN, 20ºW–60ºW). The sorted soundings and SLPs were then averaged for each SST bin for the WNP and the NA, respectively. For example, the averaged sounding and SLP over the WNP in the SST bin (27.5ºC, 28.5ºC] represents the sounding for SST of 28ºC over the WNP. Finally, we obtained four SST-dependent soundings (and SLPs) for the WNP (28–31ºC) and NA (27–30ºC), respectively. The corresponding numerical experiments with the SST-dependent soundings were conducted with the corresponding SSTs for the two basins, respectively, labeled as SST28_WNP–SST31_WNP and SST27_NA–SST30_NA. Similarly, in addition to the standard experiments with all default settings as described above, to examine the effect of change in theoretical MPI on the dependence of superintensity on SST under the realistic atmospheric sounding, for both basins, three additional sensitivity experiments, as SST29_WNP–SST31_WNP and SST28_NA–SST30_NA but with the increase of theoretical MPI from SST28_WNP and SST27_NA suppressed by varying C_{D1} together with SST (similar to the method in Eq. 3), were performed, respectively.

The initial TC vortex had a radial profile of tangential wind speed with the radial shape parameter of 1.6 following Wood and White (2011). The tangential wind speed decreases linearly with height from the maximum (V_{max}) of 15 m s^{-1} at the surface to zero at 18-km height, with the radius of maximum wind (RMW) of 80 km in the standard run of each experiment. To minimize the effect of model internal variability on our main conclusions and ensure the robustness of the model results and the findings, 21 ensemble runs for each experiment were performed with the perturbed initial RMW and the initial V_{max}, similar to those used in Li et al. (2020). Namely, in addition to the standard run, each of the remaining 20 runs were generated by perturbing the initial RMW by an increment of ±0.4 km (for 10 runs) or the initial V_{max} by ±0.1 m s^{-1} (for 10 runs). Although a non-negligible variability exists for both the maximum intensity and RMW during the quasi-steady state in each experiment, with an averaged standard deviation of about 4 m s^{-1} and 1 km (shown in those time evolution figures), respectively, our preliminary tests indicate that the ensemble-mean results discussed herein are robust and insensitive to the perturbation increments within reasonable ranges. Note that the experiments with the Dunion (2011)'s sounding were integrated for 120 h while those with the SST-dependent soundings were integrated for 240 h to ensure all runs reached their quasi-steady state. The results discussed below were based on the ensemble mean from the hourly model outputs for each experiment.

3. Superintensity with the SST-independent sounding

Figure 1 shows the time evolutions of the maximum 10-m total wind speeds of all individual ensemble runs and ensemble mean and their corresponding RMWs for each SST experiment using the initial atmospheric sounding of Dunion (2011). Both the intensification rate (Fig. 1a) and the contraction rate of the RMW (Fig. 1b) during the intensification period increase with increasing SST, consistent with previous modeling results using SST-independent atmospheric sounding (e.g., Črnivec et al. (2016). Note that the RMW contraction stopped well before the end of intensification period in each experiment, which is consistent with the observational analysis of Stern et al. (2015) and the modeling results of Stern et al. (2015) and Li et al. (2019). The time reaching the quasi-steady state decreases and the quasi-steady intensity increases with increasing SST (Fig. 1a).

Figure 2a shows the steady-state intensity of the simulated TC and the corresponding theoretical MPI as a function of SST. Here, the steady-state intensity was an average of the ensemble mean maximum 10-m wind speed in the period of 96–120 h for each experiment. The theoretical MPI was calculated using Eq. (1) with all variables diagnosed directly from the model output and averaged in the same time period of 96–120 h. Following Rousseau-Rizzi and Emanuel (2019), the outflow temperature was calculated as the temperature at the intersection of the zero-azimuthal-wind contour and the absolute angular momentum surface across the maximum wind speed point in the ensemble mean. The simulated quasi-steady TC intensity increases with SST at a rate of ~3.4 m s^{-1} $^{o}C^{-1}$, which is much smaller than the rate of ~6 m s^{-1} $^{o}C^{-1}$ of the theoretical MPI (Fig. 2a). The simulated steady-state intensity is larger than the theoretical MPI at SSTs lower than ~29.5°C but becomes smaller than at SSTs above ~29.5°C. Namely, the simulated steady-state intensity changes from superintensity to sub-MPI intensity at SST≈29.5°C. This indicates a strong dependence of superintensity on SST (Fig. 2b). Note that here as in Rousseau-Rizzi and Emanuel (2019), the superintensity is defined as the normalized excess of maximum 10-m wind speed of the simulated TC in the steady-state relative to the theoretical MPI [i.e., $SI = (SV_{max} - |\boldsymbol{V}_{MPI}|)/|\boldsymbol{V}_{MPI}|$, where SV_{max} is the ensemble-mean steady-state intensity as defined above]. We can see from Fig. 2b that the superintensity decreases with increasing SST, from ~18% at SST= 27°C to zero at SST≈29.5°C, and then becomes negative ~-9% (sub-MPI) at SST=32°C. Similar superintensity at SSTs lower than 29.5°C has been reported in previous studies using the Dunion (2011)'s mean tropical atmospheric sounding (Bryan 2012; Peng et al. 2018; Tao et al. 2019).

However, the superintensity is considerably larger in this study than that in Rousseau-Rizzi and Emanuel (2019), who found the superintensity of 5% only in the nearly inviscid limit for SST of 27°C. Note that the horizontal mixing length of 700 m used in this study was in the sub-MPI regime of Rousseau-Rizzi and Emanuel (2019), who showed that sub-MPI intensity occurs when the horizontal mixing length is greater than ~500 m. The different degrees of superintensity between the two studies could be due to various factors. The first possible factor could be the difference in the initial atmospheric sounding. The initial sounding used in this study for SST at 27°C implies an environmental CAPE of ~2000 J Kg^{-1} while the initial atmospheric sounding used in Rousseau-Rizzi and Emanuel (2019) was neutral to convection (with nearly zero environmental CAPE). However, the air-sea temperature difference near the surface in Rousseau-Rizzi and Emanuel (2019) (~3.5°C) was much larger than in this study (~0.2°C), implying a larger production rate of CAPE. Given that high environmental CAPE favors the enhancement of convective activity in the outer region and may be negative to TC intensification and limit the maximum TC intensity as previously demonstrated by Wang (2009), the higher production rate of CAPE in the TC environment and thus the convective activity in the outer region may likely contribute to the smaller superintensity for the same SST in Rousseau-Rizzi and Emanuel (2019) than in this study, which was verified by an additional sensitivity experiment as SST27 but using the initial atmospheric sounding in Rousseau-Rizzi and Emanuel (2019) (not shown). Another factor that could be responsible for the different degrees of superintensity between the two studies is the different algorithms used in calculating the surface enthalpy disequilibrium. In Rousseau-Rizzi and Emanuel (2019), the surface enthalpy disequilibrium was approximated as the moist static energy difference between the top of the boundary layer and the ocean surface. However, in this study it was directly diagnosed from the model output of surface enthalpy flux, which was smaller than that using the algorithm of Rousseau-Rizzi and Emanuel (2019) (not shown). This suggests that the enthalpy disequilibrium at the air-sea interface and thus the theoretical MPI in Rousseau-Rizzi and Emanuel (2019) could be overestimated, partly leading to the underestimated superintensity. In addition, partly because Rousseau-Rizzi and Emanuel (2019) used a larger C_k and smaller C_D ($C_k = C_D = 0.002$) and with the inclusion of dissipative heating, the theoretical MPI in their simulations for SST at 27°C with the horizontal mixing length around 700 m is much higher (~90 m s^{-1}; see their Fig. 5) than in this study (~45 m s^{-1}; Fig. 2a), which could also contribute to a smaller superintensity (shown below). Some other factors include the use of coarser horizontal grid spacing (2 km in the inner region), uniform vertical grid spacing of 300 m, warm rain cloud microphysics scheme with a constant terminal velocity of precipitating drops, and so on, in the CM1 simulations of Rousseau-Rizzi and Emanuel (2019). Besides, Rousseau-Rizzi and Emanuel (2019) used single simulations rather than ensemble simulations, in which the results tend to be sensitive to any other small initial perturbations, as implied by the non-negligible standard deviation in Fig. 1a. Therefore, a direct comparison of the degree of superintensity between the two studies seems not to be straightforward. A detailed analysis is beyond the scope of this study but could be a topic for a future work.

Since the theoretical MPI assumes a balance between the surface available power production and power dissipation near the RMW (Emanuel 1997; Rousseau-Rizzi and Emanuel 2019), the superintensity thus implies an imbalance between the two by definition. Therefore, it is our interest to examine the time evolution of the available power production and power dissipation near the RMW and their radial distributions in the steady state of the simulated TCs in all SST experiments, as done in Wang and Xu (2010). The surface available power production per unit area (PD) and the frictional dissipation per unit area (DS) as a function of radius (*r*) and time (*t*) can be written as

$$\mathrm{PD}(r,t) = [\rho\epsilon T_s C_k |\boldsymbol{V}|(s_0^* - s_b)]|_{r,t}, \tag{4a}$$

$$\mathrm{DS}(r,t) = [\rho C_D |\boldsymbol{V}|^3]|_{r,t}, \tag{4b}$$

where ρ is the air density near the ocean surface and other variables have their meanings same as in Eqs. (1) and (2). Note that the thermodynamic efficiency is a system efficiency and thus is radius-independent. Figure 3 shows the evolutions of the diagnosed PD (red asterisk) and DS (blue asterisk) at the RMW as a function of the TC intensity ($|\boldsymbol{V}|_{RMW}$) based on the model output in different SST experiments. Consistent with Eq. (4), the PD nearly increases linearly with the TC intensity (red line), because the change of both the thermodynamic efficiency ϵ and the air-sea thermodynamic disequilibrium $[\rho T_s C_k (s_0^* - s_b)]$ with time are very small compared with the TC intensity (not shown), while the DS increases as a cubic function of the TC intensity (blue line). Therefore, although the PD is greater than the DS at lower intensity, the DS increases much faster than the PD as the storm intensifies, and eventually the PD and DS intersect at some high intensity, which is regarded as the theoretical MPI by definition (Wang 2012), determined by Eq. (1). In the experiments with SSTs of 27–29ºC (Figs. 3a–c), as the TC intensity increases, the PD and DS at the RMW intersect but the DS is greater than the PD in the steady state, indicating the superintensity by definition (Fig. 2b). For SST of at 30ºC and above, the curves of the PD and DS at the RMW do not intersect, with the PD being greater than the DS in the steady state (Figs. 3d-f), indicating the sub-MPI intensity by definition (Fig. 2b).

Wang and Xu (2010) indicated that the superintensity is related to the negative imbalance between the PD and DS (PD<DS) under the eyewall, which could be supplemented by the inward transport of power production outside the eyewall. Namely, in addition to the primary power production under the eyewall, the power production in the near-core environment outside the RMW, where the available power production is often larger than the production dissipation (Fig. 4), could be an extra energy source to the TC system and balance the power dissipation under the eyewall (Figs. 4a–c). However, the negative imbalance (and thus the superintensity) decreases with increasing SST. The TC reached a steady-state intensity even with the positive imbalance (PD>DS) under the eyewall at SSTs of 30ºC and above (Figs. 4d–f). This suggests that the excess available power production was not effective to further intensify the TC in these experiments with relatively high SSTs. We hypothesize that the efficiency of the available power production decreases in intensifying the TC with increasing SST but increases in spinning up tangential wind outside the RMW and thus increasing the TC size.

As already mentioned in Section 2, for a given SST-independent initial atmospheric sounding, the air-sea thermodynamic disequilibrium and thus surface enthalpy flux would increase rapidly with increasing SST. The increase in air-sea thermodynamic disequilibrium $[\rho T_s C_k (s_0^* - s_b)]$ with increasing SST is shown in Fig. 5, which shows the radial distribution of the ensemble mean air-sea thermodynamic disequilibrium averaged between 96–120 h in different SST experiments. Note that as implied from Fig. 3 and mentioned above, the air-sea thermodynamic disequilibrium in each experiment changed very marginally with time. Consistent with the increasing air-sea thermodynamic disequilibrium in the TC outer region, convective activity in the outer region (mainly outside about 2–2.5 times of the RMW) becomes increasingly more active with increasing SST as inferred from the precipitation rate shown in Fig. 6. This is because that a higher air-sea thermodynamic disequilibrium (or surface enthalpy flux) implies faster production rate of CAPE or convective instability (Emanuel 1994), and thus a condition more favorable for the development of convection in the TC environment, which is maintained via consuming CAPE. Diabatic heating in the outer region facilitates the low-level inflow to spin up tangential wind outside the eyewall, increasing the TC size (Wang 2009; Xu and Wang 2010), but reduces the inflow toward the eyewall and thus weakens the eyewall updraft, limiting the TC intensification and final intensity (Bister 2001; Wang 2009). This means that the contribution of available power production to TC intensification and final intensity decreases while that to the TC size increases with increasing SST due to the gradual increase in the production rate of CAPE and convective activity in the outer region as SST increases. As expected, although the superintensity decreases with increasing SST, the TC inner–core size in the quasi-steady state increases as SST increases (Fig. 1b). The overall size increase can be inferred from the outward expansion of low-level tangential wind outside the eyewall, which increases as SST increases (Fig. 6). This is similar to that found in Sun et al. (2017), who attributed such a size increase with increasing SST to the enhanced rainband and convective activity in the TC outer region as previously demonstrated by Wang (2009) and Xu and Wang (2010). Therefore, the strong dependence of the superintensity on SST can be partly explained by the rapidly increasing convective activity in the TC outer region resulting from the increasing air-sea thermodynamic disequilibrium under the given SST-independent initial atmospheric sounding. This will be further confirmed by results with more realistic SST-dependent initial atmospheric soundings in Section 4.

On the other hand, the theoretical MPI, i.e., the denominator of the definition for superintensity, also increases with SST as in Eq. (1) and Fig. 2. Considering that the storm with higher theoretical MPI requires stronger radial gradients of entropy and angular momentum, which are more affected by parameterized turbulence, a question arises as to whether the decrease of superintensity with increasing SST is caused by the increasing theoretical MPI, or whether the storm with higher theoretical MPI could be less likely to reach or exceed their MPI in simulations under the same turbulence mixing length. To address this issue, five additional sensitivity experiments as SST28–SST32 but with different C_{D1} were performed (Fig. 7a) as introduced in Section 2. By varying SST and C_{D1} simultaneously, the theoretical MPI in each sensitivity experiment was almost unchanged from SST27 (Fig. 7c) and the changes of the air-sea thermodynamic disequilibrium (Fig. 7b) and thus precipitation rate (not shown) were retained as those experiments with fixed C_{D1} (Fig. 5 and Fig. 6). As expected, although with a similar theoretical MPI, the simulated steady-state intensity decreases with increasing SST (Fig. 7a,c), and thus the superintensity also decreases (Fig. 7d), consistent with the rapidly increasing air-sea thermodynamic disequilibrium (Fig. 7b) and thus convective activity (not shown) in the TC outer region. However, the intersection between the simulated steady-state intensity and the theoretical MPI indeed shifts to a higher temperature ~31°C (Fig. 7c) from ~29.5 °C in the experiments with fixed C_{D1} (Fig. 2a), and the averaged decreasing rate of superintensity with increasing SST is now reduced, but slightly (~15%) to ~4.6 % °C^{-1} (Fig. 7d) from ~5.4 % °C^{-1} (Fig. 2b). This means that although the storms with higher theoretical MPI indeed could be less likely to reach or exceed their MPI in simulations, and thus the decrease of superintensity with increasing SST is partly caused by the increasing theoretical MPI, it is the rapidly increasing convective activity in the TC outer region resulting from the rapidly increasing air-sea thermodynamic disequilibrium that dominates the decrease of superintensity in the SST-independent sounding experiments.

4. Superintensity with SST-dependent soundings

Results discussed in Section 3 suggest a strong dependence of superintensity on SST in the SST-independent initial sounding experiments primarily due to the strong SST-dependent convective activity in the TC outer region. This means that the dependence of superintensity on SST could become negligible or reduced if the dependence of convective activity in the TC outer region on SST is suppressed. To address this issue, we performed another set of experiments using the SST-dependent initial atmospheric soundings based on observations in the WNP and NA (see Section 2). Figure 8 shows the SST-dependent atmospheric soundings and their corresponding initial CAPEs over the WNP and NA, respectively. We can see that the initial sounding over the WNP shows a slightly larger CAPE than over the NA for a same SST. Unlike in the SST-independent sounding experiments, the initial CAPEs in both basins increase with SST, which may indicate a larger increasing rate of convective activity in the TC outer region with increasing SST than that in the SST-independent sounding experiments. However, the initial CAPE of any SST-dependent sounding is smaller than that in the SST-independent sounding experiments, and the increasing rate of initial CAPE is slightly larger (~293 J Kg^{-1} $^{o}C^{-1}$) in the NA than that (~150 J Kg^{-1} $^{o}C^{-1}$) in the WNP. More importantly, the dependences of the air-sea thermodynamic disequilibrium in the TC outer region (mainly outside about 2–2.5 times of the RMW) on SST in the SST-dependent sounding experiments (Fig. 9) are much smaller than that in the SST-independent sounding experiments shown in Fig. 5, but with a similar dependence in the near-core region. Therefore, results from this section may help confirm whether the strong SST-dependent superintensity in the SST-independent sounding experiments discussed in Section 3 is primarily due to the strong SST-dependent convective activity in the TC outer region and whether the steady-state intensity of the simulated TC depends on the air-sea thermodynamic disequilibrium in the outer region or the production rate of environmental CAPE for a given SST.

To address the above issues, we first examine the convective activity in all SST-dependent sounding experiments. As we can see from Fig. 10, although there is an increase of convective activity in the TC outer region with increasing SST, its increasing rate is much smaller in the more realistic SST-dependent sounding experiments over both the WNP and NA, compared with that in the SST-independent sounding experiments discussed in Section 3 (Fig. 6). This is consistent with the smaller dependence of the air-sea thermodynamic disequilibrium in the TC outer region on SST in the former than in the latter (Figs. 9 and 5) as mentioned above. This suggests that the relatively weak dependence of the air-sea thermodynamic disequilibrium and thus convective activity in the TC outer region on SST would largely suppress the SST-dependence of superintensity in the SST-independent sounding experiments discussed in section 3.

Figures 11a–c show the time evolutions of the simulated TC intensity and the corresponding steady-state (averaged in the same time period of 180–240 h) intensity and theoretical MPI as a function of SST in all experiments with the SST-dependent atmospheric soundings over the WNP and NA, respectively. Both the intensification rate and steady-state intensity of the simulated TCs increase with increasing SST for the initial soundings of both basins (Figs. 11a-c), which is consistent with observations documented by Xu and Wang (2018). Similarly, the theoretical MPI also shows an increasing tendency with increasing SST (Fig. 11c), and the increasing rate in both the SST-independent sounding experiments and the SST-dependent sounding experiments are similar (~6 m s^{-1} $^{o}C^{-1}$; Figs. 2a and 11c), because the air-sea thermodynamic disequilibrium under the eyewall, which determines the theoretical MPI (Eq. 1), show a similar dependence on SST among those two sets of experiments, as mentioned above (Figs. 5 and 9). However, unlike in the SST-independent sounding experiments discussed in Section 3 (Fig. 2a), the increasing rates of the steady-state intensity are also similar to the corresponding theoretical MPI with increasing SST at ~5–6.5 m s^{-1} $^{o}C^{-1}$ (Fig. 11c), and the increasing rates for the WNP and NA sounding experiments are very close to each other. Note that both the theoretical MPI and the steady-state intensity at a same SST are slightly higher in experiment with the NA sounding than with the WNP sounding (Fig. 11c), mainly because the inner-core air-sea thermodynamic disequilibrium in the WNP sounding experiment is smaller than in the NA sounding experiment for a same SST (Fig. 9). This is consistent with the results of Xu et al. (2019), who found the slightly higher MPI over the NA than over the WNP for a same SST is due to the warmer troposphere and wetter boundary layer over the WNP, as shown in Fig. 9. This suggests that there is a competition between the positive role of the inner-core air-sea thermodynamic disequilibrium and the negative role of the air-sea thermodynamic disequilibrium in the outer region in determining the TC steady-state intensity. In addition, these results, together with those from Section 3, strongly suggest that both the TC steady-state intensity and the theoretical MPI may not depend on the initial environmental CAPE, consistent with Persing and Montgomery (2005). For example, for SST=28^{o}C, the steady-state TC intensities and theoretical MPIs using both the initial sounding of Dunion (2011) and that over the NA are greater than those over the WNP (Figs. 2a and 11c), but the initial CAPEs in Dunion (2011) and over the NA are greater and smaller than the initial CAPE over the WNP (Fig. 8), respectively.

Although the superintensity also decreases with increasing SST (Fig. 11d), the decreasing rate is largely reduced in the SST-dependent sounding experiments compared with that in the SST-independent sounding experiments discussed in Section 3. The averaged decreasing rate of superintensity with increasing SST is now reduced by ~60% to ~2.2 % $^{o}C^{-1}$ for the WNP and by ~45% to ~3 % $^{o}C^{-1}$ for the NA from ~5.4 % $^{o}C^{-1}$ in the SST-independent sounding experiments (Fig. 2b). Because the increasing rate of theoretical MPI with increasing SST is almost the same between the SST-independent (Fig. 2a) and SST-dependent (Fig. 11c) sounding experiments as mentioned above (~6 m s^{-1} $^{o}C^{-1}$), the smaller decreasing rate of superintensity in the latter is thus mainly a result of the suppressed increasing tendency of convective activity in the TC outer region (Fig. 6 and Fig. 10). The difference in the decreasing rate of superintensity with increasing SST between the two sounding experiments, for the same SST range (28–30ºC), is small (Fig. 11d). This is consistent with the small difference in the dependence of air-sea thermodynamic disequilibrium (and thus convective activity) in the TC outer region (Figs. 9 and 10) on SST between the WNP and NA soundings. Note also that the sub-MPI steady-state intensity in the SST-independent sounding experiments at high SSTs did not occur in the SST-dependent sounding experiments. These results further confirm that the air-sea thermodynamic disequilibrium and thus the production rate of CAPE in the outer region are detrimental to the steady-state intensity of the simulated TC, while such a detrimental effect on the theoretical MPI (dominated by the inner-core air-sea thermodynamic disequilibrium) is slightly weaker, resulting in an increase in superintensity with increasing SST in the SST-independent sounding experiments.

In addition, considering that the increase of theoretical MPI with increasing SST would also reduce the superintensity as analyzed above, and the increasing convective activity in the TC outer region with increasing SST is much small in the SST-dependent sounding experiments (Fig. 10), it is hypothesized that the slightly decreasing rate of superintensity with increasing SST in the SST-dependent sounding experiments (Fig. 11d) would be dominated by the increase of theoretical MPI rather than the increasing convective activity in the outer region with increasing SST in the SST-dependent sounding experiments. To verify this, for both basins, three additional sensitivity experiments as SST29_WNP–SST31_WNP and SST28_NA–SST30_NA but with the increase of theoretical MPI from SST28_WNP and SST27_NA suppressed by varying C_{D1} together with SST were performed (Section 2), respectively. As we can see from Fig. 12a, both the simulated steady-state intensity and theoretical MPI show a marginal change with C_{D1} varied for both basins. As a result, although the superintensity still decreases with increasing SST for both basins (Fig. 12b), their averaged decreasing rates for the WNP and NA are reduced from ~2.2 % $^{o}C^{-1}$ and ~3 % $^{o}C^{-1}$ to ~0.3 % $^{o}C^{-1}$ and ~1.2 % $^{o}C^{-1}$ or by ~86% and ~60%, respectively, in the experiments with default C_{D1} (Fig. 11d). Therefore, these results, together with those from Section 3, strongly suggest that the increases in both convective activity in the TC outer region and theoretical MPI with increasing SST could reduce the superintensity. When there is a rapid increase in the air-sea thermodynamic disequilibrium and thus the production rate of CAPE in the TC outer region with increasing SST as in the SST-independent sounding experiments, it is the increasing convective activity in the outer region that dominates the decrease of superintensity with increasing SST, otherwise it is the increasing theoretical MPI that dominates the decrease of superintensity with increasing SST as in the SST-dependent sounding experiments.

5. Conclusions and discussion

Previous studies have shown the existence of superintensity of numerically simulated TCs under favorable environmental conditions. However, the dependence of the degree of superintensity on various environmental conditions, model settings, and physical parameters/processes has not been fully investigated. In this study, the dependence of superintensity on SST has been examined using ensemble axisymmetric model simulations with both the SST-independent and SST-dependent initial atmospheric soundings. Following Rousseau-Rizzi and Emanuel (2019), we also defined the superintensity as the proportion of the excess maximum surface wind speed of the simulated TC to the corresponding theoretical MPI, namely, the excess steady-state intensity normalized by the corresponding theoretical MPI in terms of maximum surface wind speed.

In the SST-independent sounding experiments, the superintensity occurs in relatively low SST experiments with less active convective activity in the TC outer region but sub-MPI intensity (or negative superintensity) occurs in relatively high SST experiments with strong convective activity in the outer region. We show that the superintensity occurs when the power dissipation is larger than the available power production locally under the eyewall in the steady state, consistent with the definition of superintensity in the MPI theory. Therefore, the superintensity implies the importance of the extra power production imported from outside of the RMW to balance the power dissipation under the eyewall, which was not considered in the theoretical MPI, consistent with the finding of Wang and Xu (2010). The sub-MPI intensity at high SSTs results primarily from the excessive convective activity in the TC outer region due to the rapid increase in environmental CAPE resulting from the increasing surface enthalpy flux associated with the increasing air-sea thermodynamic disequilibrium with increasing SST because of the use of the same initial atmospheric sounding.

A new finding is a robust decrease of superintensity with increasing SST no matter in experiments with the SST-independent sounding or those with the realistic SST-dependent soundings based on observations over the WNP and NA. It is found that the increasing convective activity (and thus diabatic heating) in the TC outer region with increasing SST could result in the decrease of superintensity. As a result, because of the more pronounced increasing convective activity in the TC outer region with increasing SST in the SST-independent sounding experiments than in the SST-dependent sounding experiments, the decreasing rate of superintensity with increasing SST is considerably larger in the former experiments than in the latter experiments. The more rapid increasing convective activity in the TC outer region with increasing SST is due to the rapid increase in air-sea thermodynamic disequilibrium as mentioned above. Although the initial CAPE increases with increasing SST in experiments with the realistic initial atmospheric soundings constructed based on observations over the NA and WNP, the CAPE itself and the increasing rate of the production rate of CAPE with increasing SST is much smaller than in the SST-independent sounding experiments. As a result, the decreasing rate of superintensity with increasing SST is largely suppressed in the realistic sounding experiments. The averaged decreasing rate of superintensity with increasing SST is ~2.2 % $^{o}C^{-1}$ for the WNP soundings and ~3 % $^{o}C^{-1}$ for the NA soundings, and ~5.4 % $^{o}C^{-1}$ in the SST-independent sounding experiments.

In addition, it is found that the increasing theoretical MPI could also reduce the superintensity with increasing SST, which is verified by additional sensitivity experiments with the increase of theoretical MPI with increasing SST suppressed by varying the upper limit of drag coefficient together with SST. Although the effect of the increasing theoretical MPI with increasing SST in the SST-independent sounding experiments is minor, it dominates the decrease of superintensity in the SST-dependent sounding experiments with the increasing rate of air-sea thermodynamic disequilibrium and thus convective activity in the TC outer region suppressed. This means that the storm with higher theoretical MPI could be less likely to reach or exceed their MPI in simulations. Note that this conclusion seems to be inconsistent with the result of Rousseau-Rizzi and Emanuel (2019), which shows that the increasing theoretical MPI was associated with an increase in superintensity with decreasing horizontal mixing length. This is because a smaller horizontal mixing length and thus a lower turbulent mixing implies stronger radial gradients of entropy and angular momentum and thus stronger intensity in simulations (e.g., Bryan and Rotunno 2009b; Rousseau-Rizzi and Emanuel 2019). Therefore, one possible reason for the smaller superintensity with higher theoretical MPI under the same turbulence mixing lengths in our simulations is that the storm with higher theoretical MPI requires stronger radial gradients of entropy and angular momentum, which are more affected by parameterized turbulence. However, the detailed mechanism is beyond this study and left for future work. Note that although the superintensity increases with decreasing horizontal mixing length, our additional experiments with varying horizontal mixing length showed that our main conclusion (i.e., superintensity decreases with increasing SST) is robust.

Recently, Rousseau-Rizzi and Emanuel (2019) evaluated various forms of Emanuel's theoretical MPI and showed that a new surface wind-based local Carnot cycle model proposed in Emanuel (2018) leads to the same MPI formula with the global Carnot cycle model of Emanuel (1997). Based on axisymmetric numerical simulations, Rousseau-Rizzi and Emanuel (2019) concluded that the surface wind-based MPI can give a good upper bound on the simulated TC intensity. The superintensity is only ~5 % at 27°C in the inviscid limit but becomes negative (sub-MPI) if the horizontal mixing length is greater than ~500 m. The 700 m horizontal mixing length used in this study is in the sub-MPI regime of Rousseau-Rizzi and Emanuel (2019) but results in a superintensity of 12% at the same SST with the SST-dependent sounding and of 18% with the Dunion (2011)'s mean tropical atmospheric sounding. This difference could be partly due to the different initial atmospheric soundings, the theoretical MPI itself (partly due to the differences in C_k, C_D and so on), and algorithms used in calculating the surface enthalpy disequilibrium between the two studies. In Rousseau-Rizzi and Emanuel (2019), the surface enthalpy disequilibrium was calculated according to the difference in the moist static energy between the top of the boundary layer and the sea surface. However, all the corresponding variables near the ocean surface used in the calculations of the theoretical MPI are diagnosed from the model outputs in this study. This suggests that the surface enthalpy disequilibrium, and thus the theoretical MPI in Rousseau-Rizzi and Emanuel (2019) was overestimated and thus the superintensity could be underestimated. However, several other factors may also contribute to the difference but a detailed analysis is beyond the scope of this study and could be a topic for a future study.

The robust decrease of superintensity with increasing SST in both the SST-dependent and SST-independent sounding experiments strongly suggests that caution needs to be given when one attempts to assess the possible effect of (both natural and anthropogenic) ocean warming on TC intensity and structure by numerical sensitivity experiments. Our results support a hypothesis that the efficiency of the available power production decreases in intensifying the TC with increasing SST in expense in increasingly spinning up tangential wind outside the RMW and thus increasing the TC size. Therefore, it seems that a tradeoff exists between the simulated TC intensity and TC size with the change of convective activity in the outer region as a response to the change of air-sea thermodynamic disequilibrium. Since both the TC intensity and the inner-core size are key metrics of TC disasters in terms of damaging winds and torrential rainfall, the ocean warming undoubtedly would lead to an increase in TC-induced natural disasters. In addition, our results also suggest that the degree of superintensity could be affected by the magnitude of the theoretical MPI. Since the theoretical MPI and convective activity in the TC outer region may be sensitive to various physical processes, such as the details in cloud microphysics and planetary boundary layer parameterization, it thus is not surprising that different degrees of superintensity have been reported in previous studies. Finally, note that only axisymmetric simulations were used in this study, it is unknown whether the results discussed in this study would be altered if more realistic three-dimensional simulations are conducted. Although this is a topic that needs to be addressed in future work, most of the results obtained in this study are consistent with those reported in previous studies using three-dimensional models, suggesting that the main conclusions from this study should not be changed if three-dimensional simulations are considered.

Acknowledgments: The authors thank two anonymous reviewers for their thoughtful review comments. This study was supported in part by National Natural Science Foundation of China under grants 41730960 and 41805040 and in part by the National Key R&D Program of China under grant 2017YFC1501602. Y. Wang was supported in part by NSF grant AGS-1834300 and Y. Li was funded by China Scholarship Council (File 201806210324).

References

Bister, M., 2001: Effect of peripheral convection on tropical cyclone formation. *J. Atmos. Sci.*, **58**, 3463–3476, doi:10.1175/1520-0469(2001)058<3463:EOPCOT>2.0.CO;2.

Bister, M., and K. A. Emanuel, 1998: Dissipative heating and hurricane intensity. *Meteor, Atmos. Phys*. **65**, 233-240, doi:10.1007/BF01030791.

Bister, M., and K. A. Emanuel, 2002: Low frequency variability of tropical cyclone potential intensity, 1. Interannual to interdecadal variability. *J. Geophys. Res. – Atmospheres*, **107**, 4801, doi:10.1029/2001JD000776.

Bryan, G. H., 2012: Effects of surface exchange coefficients and turbulence length scales on the intensity and structure of numerically simulated hurricanes. *Mon. Wea. Rev.,* **140**, 1125–1143, doi:10.1175/MWR-D-11-00231.1.

Bryan, G. H., and J. M. Fritsch, 2002: A benchmark simulation for moist nonhydrostatic numerical model. *Mon. Wea. Rev*., **130**, 2917-2928, doi:10.1175/1520-0493(2002)130<2917:ABSFMN>2.0.CO;2.

Bryan, G. H., and R. Rotunno, 2009a: The influence of near-surface, high-entropy air in hurricane eyes on maximum hurricane intensity. *J. Atmos. Sci.,* **66**, 148–158, doi:10.1175/2008JAS2707.1.

Bryan, G. H., and R. Rotunno, 2009b: Evaluation of an analytical model for the maximum intensity of tropical cyclones. *J. Atmos. Sci.,* **66**, 3042–3060, doi:10.1175/2009JAS3038.1.

Črnivec, N., R. K. Smith, G. Kilroy, 2016: Dependence of tropical cyclone intensification rate on sea-surface temperature. *Quart. J. Roy. Meteor. Soc.*, **142**, 1618–1627, doi:10.1002/qj.2752.

Dee, D., and Coauthors, 2011: The ERA-Interim reanalysis: Configuration and performance of the data assimilation system. *Quart. J. Roy. Meteror. Soc.* **137**, 553–597, doi:10.1002/qj.828.

DeMaria, M., and J. Kaplan, 1994: Sea surface temperature and the maximum intensity of Atlantic tropical cyclones. *J. Climate,* **7**, 1324–1334, doi:10.1175/1520-0442(1994)007<1324:SSTATM>2.0.CO;2.

Donelan, M. A., B. K. Haus, N. Reul, W. J. Plant, M. Stiassnie, H. C. Graber, O. B. Brown, and E. S. Saltzman, 2004: On the limiting aerodynamic roughness of the ocean in very strong winds. *Geophys. Res. Lett.,* **31,** L18306, doi:10.1029/ 2004GL019460.

Dunion, J. P., 2011: Rewriting the climatology of the tropical North Atlantic and Caribbean Sea atmosphere. *J. Climate*, **24**, 893-908, doi:10.1175/2010JCLI3496.1.

Emanuel, K. A., 1986: An air-sea interaction theory for tropical cyclones. Part I: Steady-state maintenance. *J. Atmos. Sci.,* **43**, 585-605, doi:10.1175/1520-0469(1986)043<0585:AASITF>2.0.CO;2.

Emanuel, K. A., 1994: *Atmospheric Convection*. Oxford University Press, 580 pp.

Emanuel, K.A., 1995: Sensitivity of tropical cyclones to surface exchange coefficients and a revised steady-state model incorporating eye dynamics. *J. Atmos. Sci.,* **52**, 3969–3976, doi:10.1175/1520-0469(1995)052<3969:SOTCTS>2.0.CO;2.

Emanuel, K. A., 1997: Some aspects of hurricane inner-core dynamics and energetics. *J. Atmos. Sci*., **54**, 1014-1026, doi:10.1175/1520-0469(1997)054<1014:SAOHIC>2.0.CO;2.

Emanuel, K., 2000: A statistical analysis of tropical cyclone intensity. *Mon. Wea. Rev.,* **128**, 1139–1152, doi:10.1175/1520-0493(2000)128<1139:ASAOTC>2.0.CO;2.

Emanuel, K., 2018: 100 Years of progress in tropical cyclone research. *Meteorological Monographs,* **59**, 15.1–15.68, doi:10.1175/AMSMONOGRAPHS-D-18-0016.1.

Frisius, T., D. Schönemann, and J. Vigh, 2013: The impact of gradient wind imbalance on potential intensity of tropical cyclones in an unbalanced slab boundary layer model. *J. Atmos. Sci.*, **70**, 1874–1890, doi:10.1175/JAS-D-12-0160.1.

Hausman, S. A., 2001: Formulation and sensitivity analysis of a nonhydrostatic, axisymmetric tropical cyclone model. Tech. rep., Air Force Institute of Technology Wright-Patterson OH.

Holland, G. J., 1997: The maximum potential intensity of tropical cyclones. *J. Atmos. Sci.,* **54**, 2519–2541, doi10.1175/1520-0469(1997)054<2519:TMPIOT>2.0.CO;2.

Jordan, C. L., 1958: Mean soundings for the West Indies area. *J. Meteor*., **15**, 91–97.

Li, Y., Y. Wang, and Y. Lin, 2019: Revisiting the dynamics of eyewall contraction of tropical cyclones. *J. Atmos. Sci*., **76**, 3229–3245, doi:10.1175/JAS-D-19-0076.1.

Li, Y., Y. Wang, and Y. Lin, 2020: How much does the upward advection of the supergradient component of boundary layer wind contribute to tropical cyclone intensification and maximum intensity? *J. Atmos. Sci.*, **77**, 2649–2664 doi:10.1175/JAS-D-19-0350.1.

Montgomery, M. T., and R. K. Smith, 2020: Comments on "An Evaluation of Hurricane Superintensity in Axisymmetric Numerical Models". *J. Atmos. Sci.*, **77**, 1887–1892, doi:10.1175/JAS-D-19-0175.1.

Montgomery, M. T., M. M. Bell, S. D. Aberson, and M. L. Black, 2006: Hurricane Isabel (2003): New insights into the physics of intense storms. Part I: Mean vortex structure and maximum intensity estimates. *Bull. Amer. Meteor. Soc*., **87**, 1335–1347, doi.org/10.1175/BAMS-87-10-1335.

Peng, K., R. Rotunno, and G. H. Bryan, 2018: Evaluation of a time-dependent model for the intensification of tropical cyclones. *J. Atmos. Sci.,* **75**, 2125–2138, doi:10.1175/JAS-D-17-0382.1.

Persing, J., and M. T. Montgomery, 2003: Hurricane superintensity. *J. Atmos. Sci.*, **60**, 2349–2371, doi:10.1175/1520-0469(2003)060<2349:HS>2.0.CO;2.

Persing, J., and M. T. Montgomery, 2005: Is environmental CAPE important in the determination of maximum possible hurricane intensity? *J. Atmos. Sci.,* **62**, 542–550, doi:10.1175/JAS-3370.1.

Rotunno, R., and K. A. Emanuel, 1987: An air-sea interaction theory for tropical cyclones. Part II: Evolutionary study using a nonhydrostatic axisymmetric numerical model. *J. Atmos. Sci*., **44**, 542-561, doi:10.1175/1520-0469(1987)044<0542:AAITFT>2.0.CO;2.

Rousseau-Rizzi, R., and K. Emanuel, 2019: An evaluation of hurricane superintensity in Axisymmetric Numerical Models. *J. Atmos. Sci.,* **76**, 1697–1706, doi:10.1175/JAS-D-18-0238.1.

Rousseau-Rizzi, R., and K. Emanuel, 2020: Reply to "Comments on 'An Evaluation of Hurricane Superintensity in Axisymmetric Numerical Models'". *J. Atmos. Sci.*, **77**, 1893–1896, doi:10.1175/JAS-D-19-0248.1.

Stern, D. P., J. L. Vigh, D. S. Nolan, and F. Zhang, 2015: Revisiting the relationship between eyewall contraction and intensification. *J. Atmos. Sci.,* **72**, 1283–1306, doi:10.1175/JAS-D-14-0261.1.

Sun, Y., Z. Zhong, T. Li, L. Yi, Y. Hu, H. Wan, H. Chen, Q. Liao, C. Ma, and Q. Li, 2017: Impact of ocean warming on tropical cyclone size and its destructiveness. *Sci Rep,* **7,** 8154, doi:10.1038/s41598-017-08533-6.

Tao, D., K. Emanuel, F. Zhang, R. Rotunno, M. M. Bell, and R. G. Nystrom, 2019: Evaluation of the assumptions in the steady-state tropical cyclone self-stratified outflow using three-dimensional convection-allowing simulations. *J. Atmos. Sci.,* **76**, 2995–3009, doi:10.1175/JAS-D-19-0033.1.

Thompson, G., P. R. Field, R. M. Rasmussen, and W. D. Hall, 2008: Explicit forecasts of winter precipitation using an improved bulk microphysics scheme. Part II: Implementation of a new snow parameterization. *Mon. Wea. Rev.,* **136**, 5095–5115, doi:10.1175/2008MWR2387.1.

Tonkin, H., G. J. Holland, N. Holbrook, and A. Henderson-Sellers, 2000: An evaluation of thermodynamic estimates of climatological maximum potential tropical cyclone intensity.

Mon. Wea. Rev., **128**, 746–762, doi:10.1175/1520-0493(2000)128<0746:AEOTEO>2.0.CO;2.

Wang, Y., 2009: How do outer spiral rainbands affect tropical cyclone structure and intensity? *J. Atmos. Sci.,* **66**, 1250–1273, doi:10.1175/2008JAS2737.1.

Wang, Y., 2012: Recent research progress on tropical cyclone structure and intensity. *Tropical cyclone Res. Rev*., **1,** 254–275, doi:10.6057/2012TCRR02.05

Wang, Y., and J. Xu, 2010: Energy production, frictional dissipation, and maximum intensity of a numerically simulated tropical cyclone. *J. Atmos. Sci.*, **67**, 97–116, doi:10.1175/2009JAS3143.1.

Whitney, L. D. and J. S. Hobgood, 1997: The relationship between sea surface temperatures and maximum intensities of tropical cyclones in the Eastern North Pacific Ocean. *J. Climate,* **10**, 2921–2930, doi:10.1175/1520-0442(1997)010<2921:TRBSST>2.0.CO;2.

Wood, V. T., and L. W. White, 2011: A new parametric model of vortex tangential-wind profiles: development, testing, and verification. *J. Atmos. Sci.,* **68**, 990–1006, doi:10.1175/2011JAS3588.1.

Xu, J., and Y. Wang, 2010: Sensitivity of tropical cyclone inner-core size and intensity to the radial distribution of surface entropy flux. *J. Atmos. Sci.*, **67**, 1831–1852, doi:10.1175/2010JAS3387.1.

Xu, J., and Y. Wang, 2018: Dependence of tropical cyclone intensification rate on sea surface temperature, storm intensity, and size in the Western North Pacific. *Wea. Forecasting,* **33**, 523–537, doi:10.1175/WAF-D-17-0095.1.

Xu, J., Y. Wang, and C. Yang, 2019: Inter-basin differences in the mean and variability of tropical cyclone MPI in the Northern Hemisphere. *J. Geophys. Res. – Atmos.,* **124**, 13714-13730, https:/doi.org/10.1029/2019JD031588.

Zhang, J. A., and M. T. Montgomery, 2012: Observational estimates of the horizontal eddy diffusivity and mixing length in the low-level region of intense hurricanes. *J. Atmos. Sci.,* **69**, 1306–1316, doi:10.1175/JAS-D-11-0180.1.

Zhang, J. A., and W. M. Drennan, 2012: An observational study of vertical eddy diffusivity in the hurricane boundary layer. *J. Atmos. Sci.,* **69**, 3223–3236, doi:10.1175/JAS-D-11-0348.1.

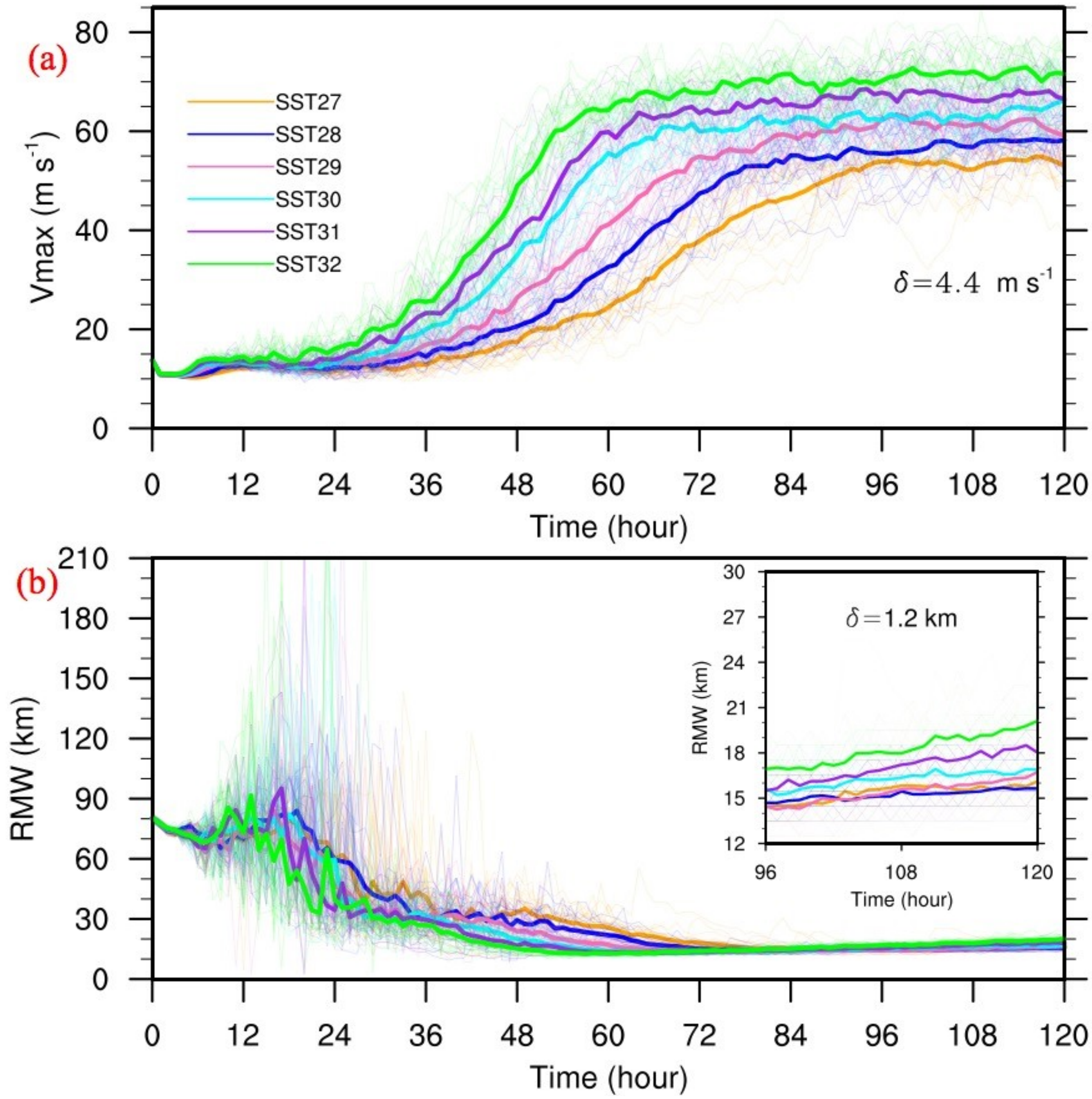

Figure 1. Time series of (a) the maximum 10-m total wind speed and (b) the corresponding radius overlaid with the zoomed-in view of the results between 96–120 h. Results from the 21 individual runs and the ensemble mean for each experiment are shown in thin and thick curves. Sigma value indicates the standard deviation for the 21 individual runs averaged among all experiments during 96–120 h.

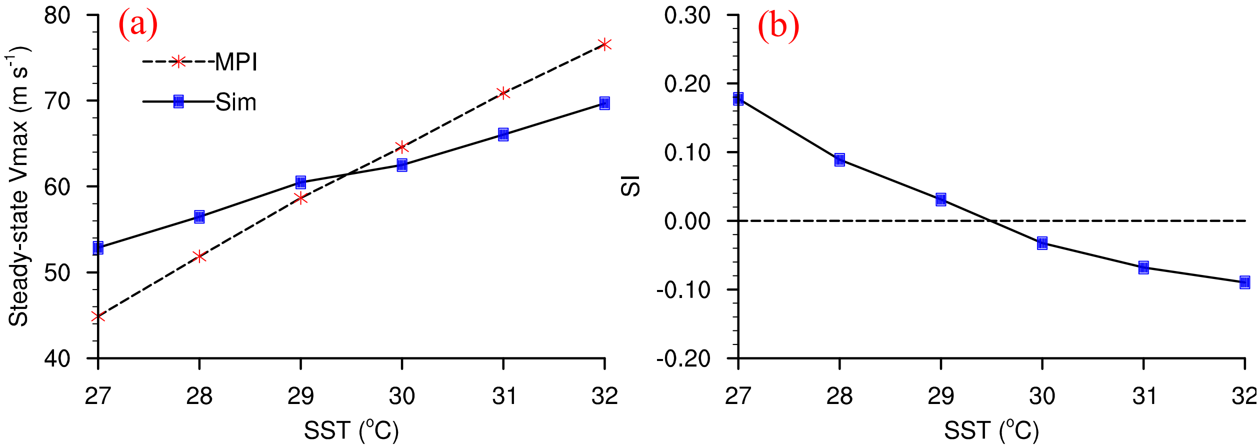

Figure 2. (a) Ensemble-mean simulated steady-state maximum 10-m total wind speed (blue, solid) and corresponding theoretical MPI (red, dashed) as a function of sea surface temperature. (b) As in (a) but showing the superintensity.

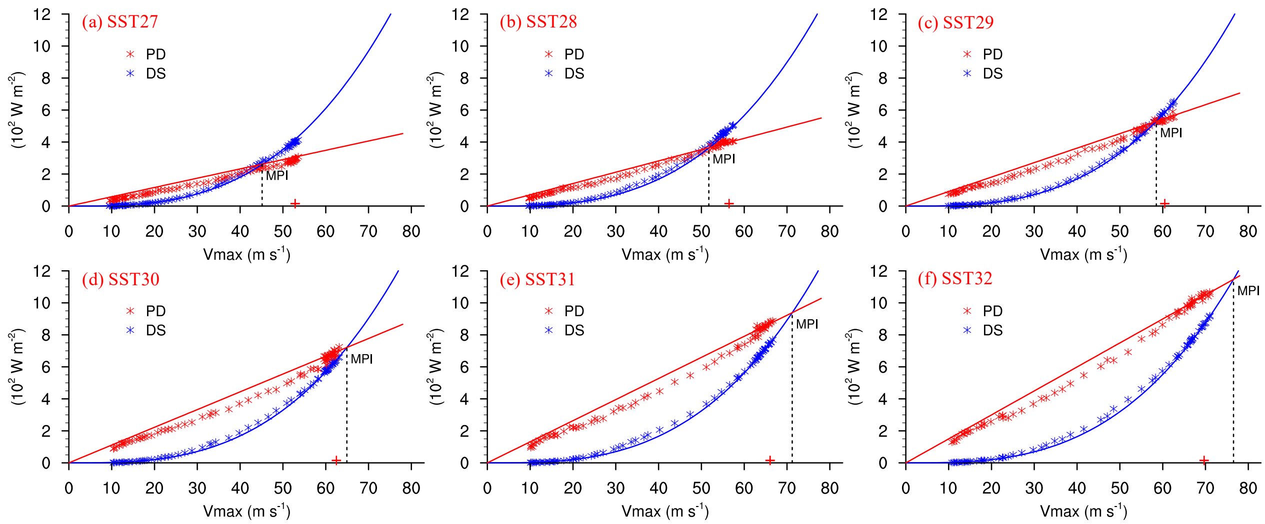

Figure 3. Ensemble-mean simulated (asterisk) and fitted (curve) available energy production rate (red) and energy dissipation rate (blue) per unit area at the location of maximum 10-m total wind speed, with the intersection between the fitted blue and red curves defined as the theoretical MPI. The simulated steady-state maximum 10-m wind speed is marked as the red plus sign near the abscissa.

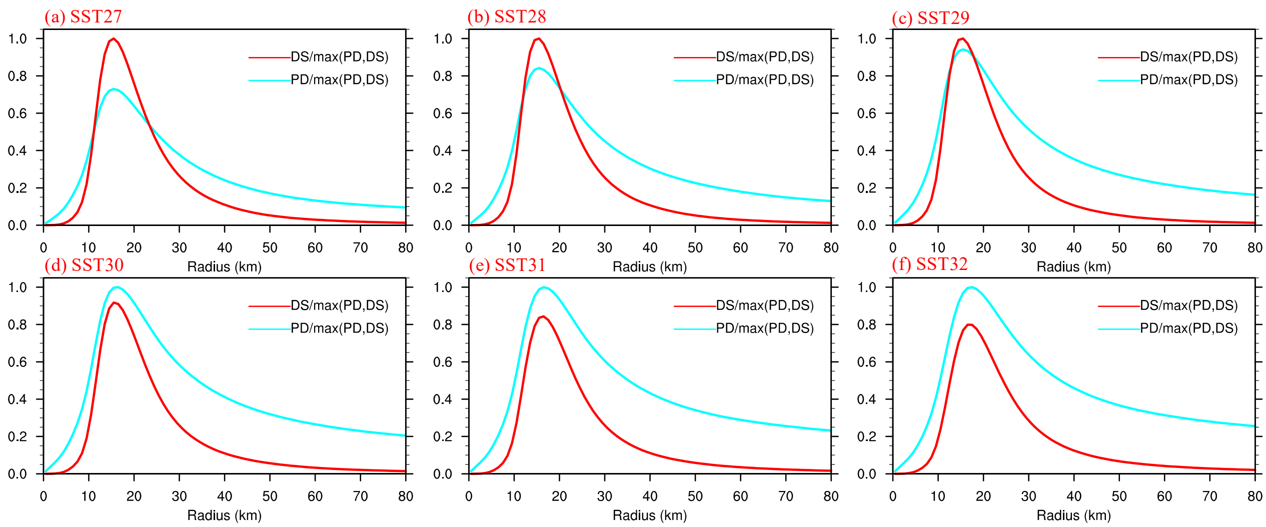

Figure 4. Radial distribution of the ensemble-mean normalized available energy production rate (cyan) and energy dissipation rate (red) per unit area averaged during the steady-state stage.

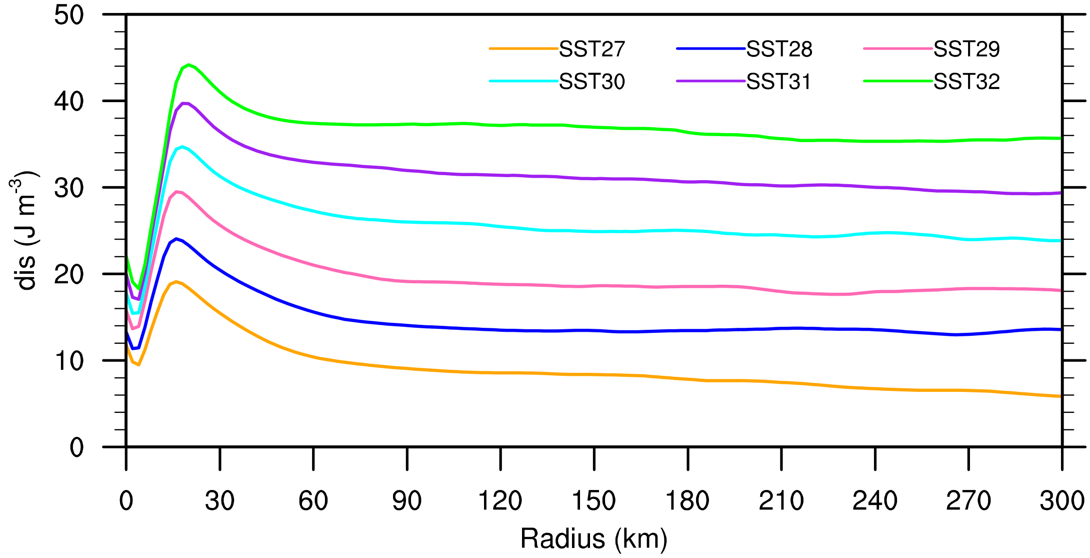

Figure 5. Radial distribution of the ensemble mean air-sea thermodynamic disequilibrium $[\rho T_s C_k(s_0^* - s_b)]$ averaged during the steady-state stage.

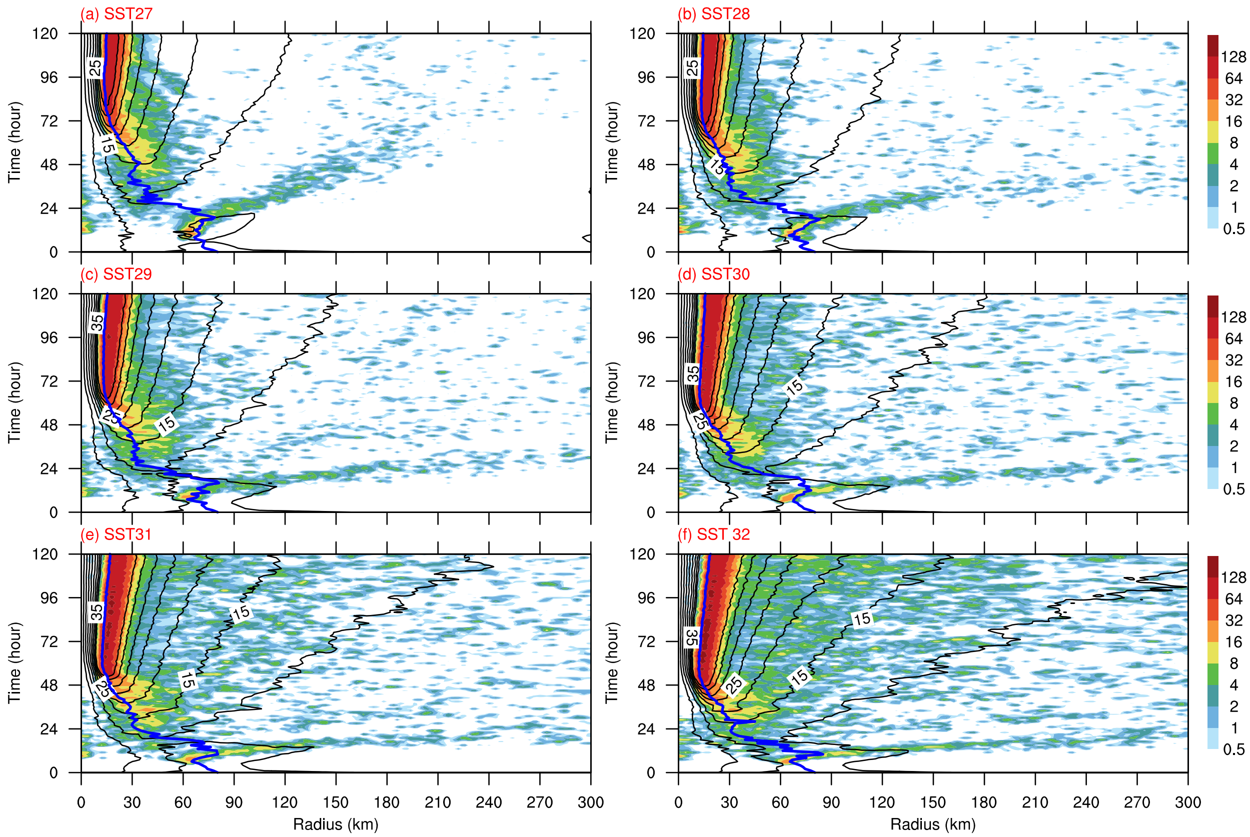

Figure 6. Radius-time Hovmöller diagram of the ensemble-mean hourly precipitation rate (shading, mm h^{-1}) and 10-m tangential wind speed (contour, at an interval of 5 m s^{-1}) with the blue line showing the location of the corresponding RMW.

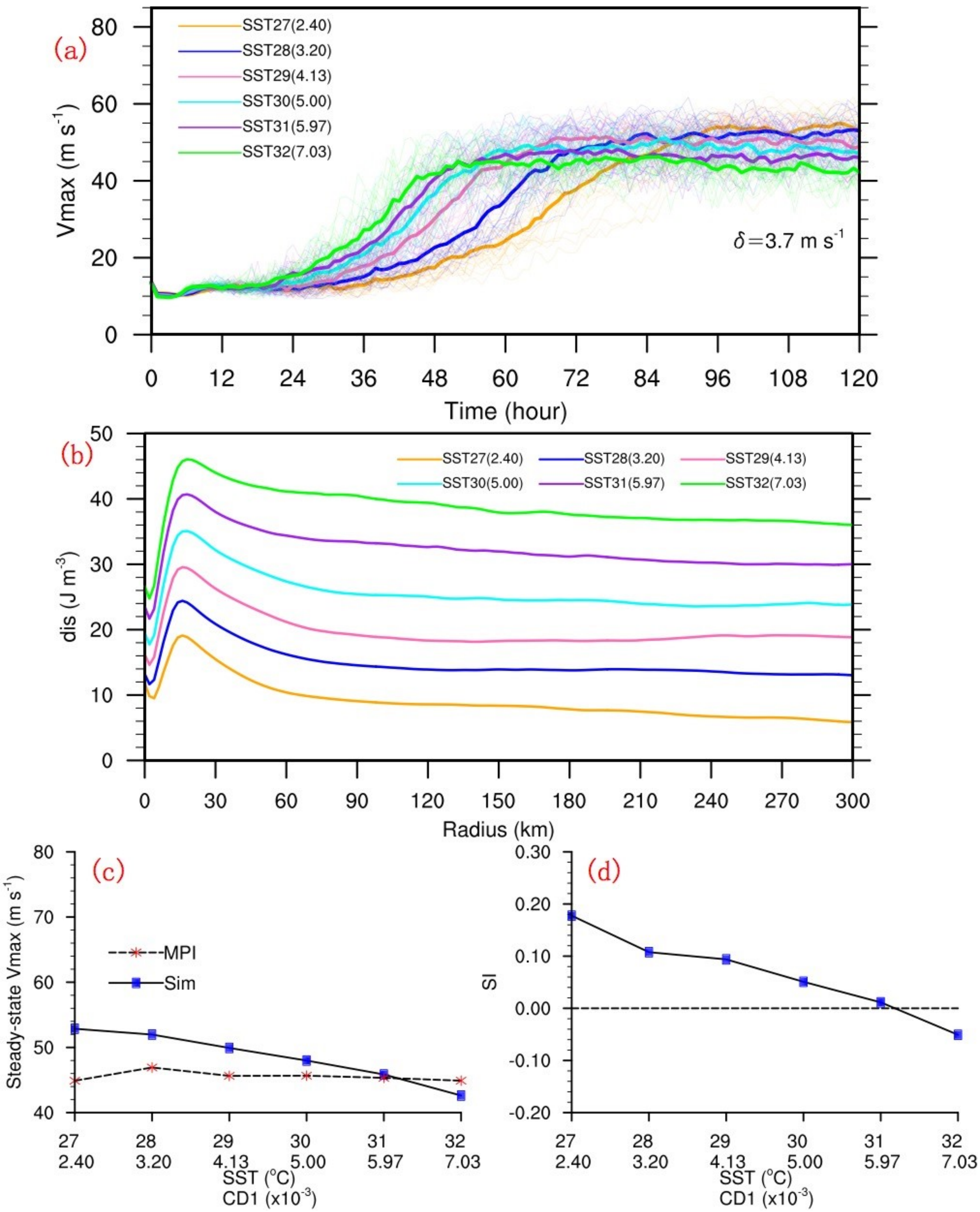

Figure 7. (a) As in Fig. 1a, (b) as in Fig. 5, and (c)–(d) as in Fig. 2a,b, but from the experiments using different upper limit of drag coefficient as shown in the brackets following the legend in (a)–(b) ($\times 10^{-3}$) and x-axis label in (c)–(d).

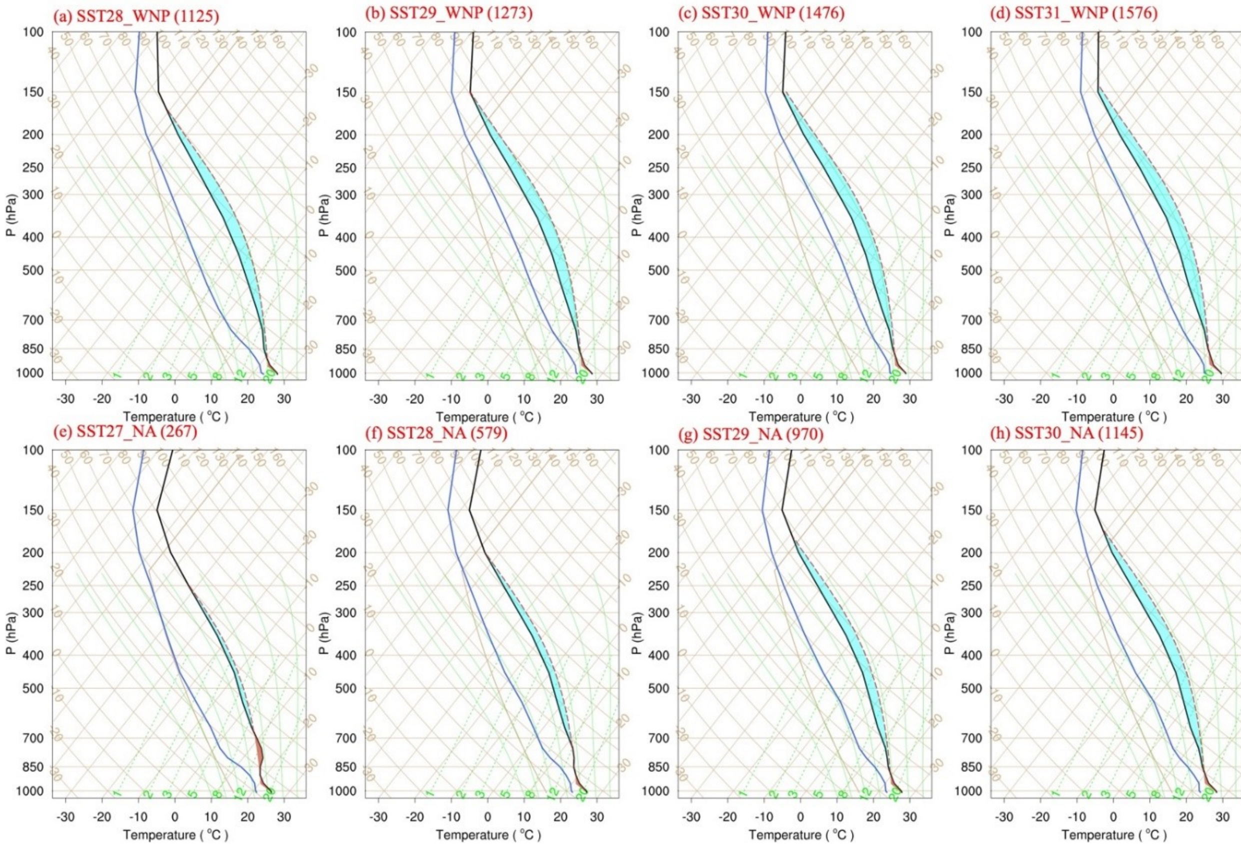

Figure 8. Skew *T*-log*p* diagram averaged over (a)–(d) the western North Pacific and (e)–(h) the North Atlantic between 2009–2018. The corresponding initial convective available potential energy (CAPE, J kg^{-1}) is shown in the brackets following the title label in each panel.

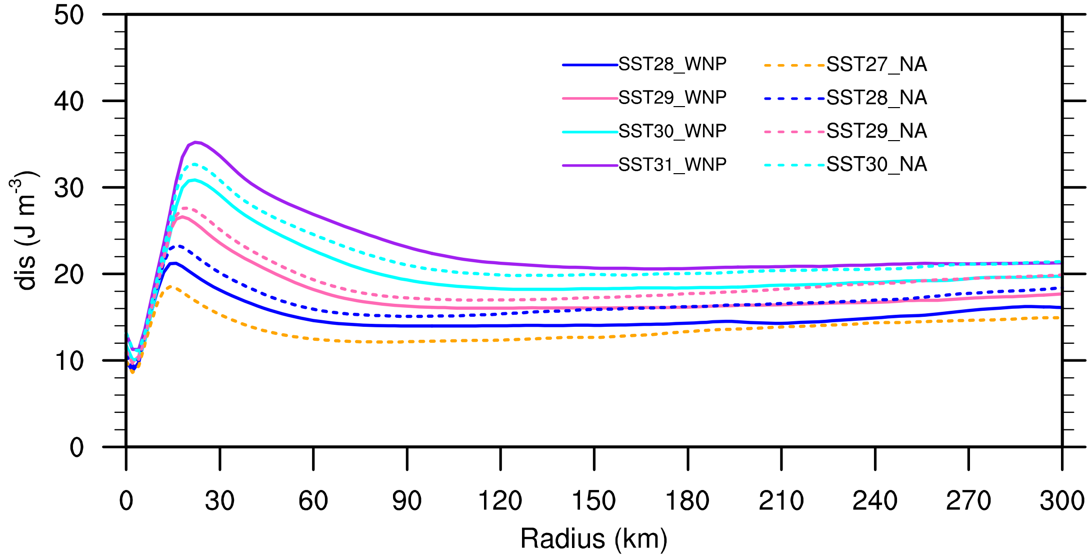

Figure 9. As in Fig. 5 but for results from the experiments using the realistic SST-dependent atmospheric soundings.

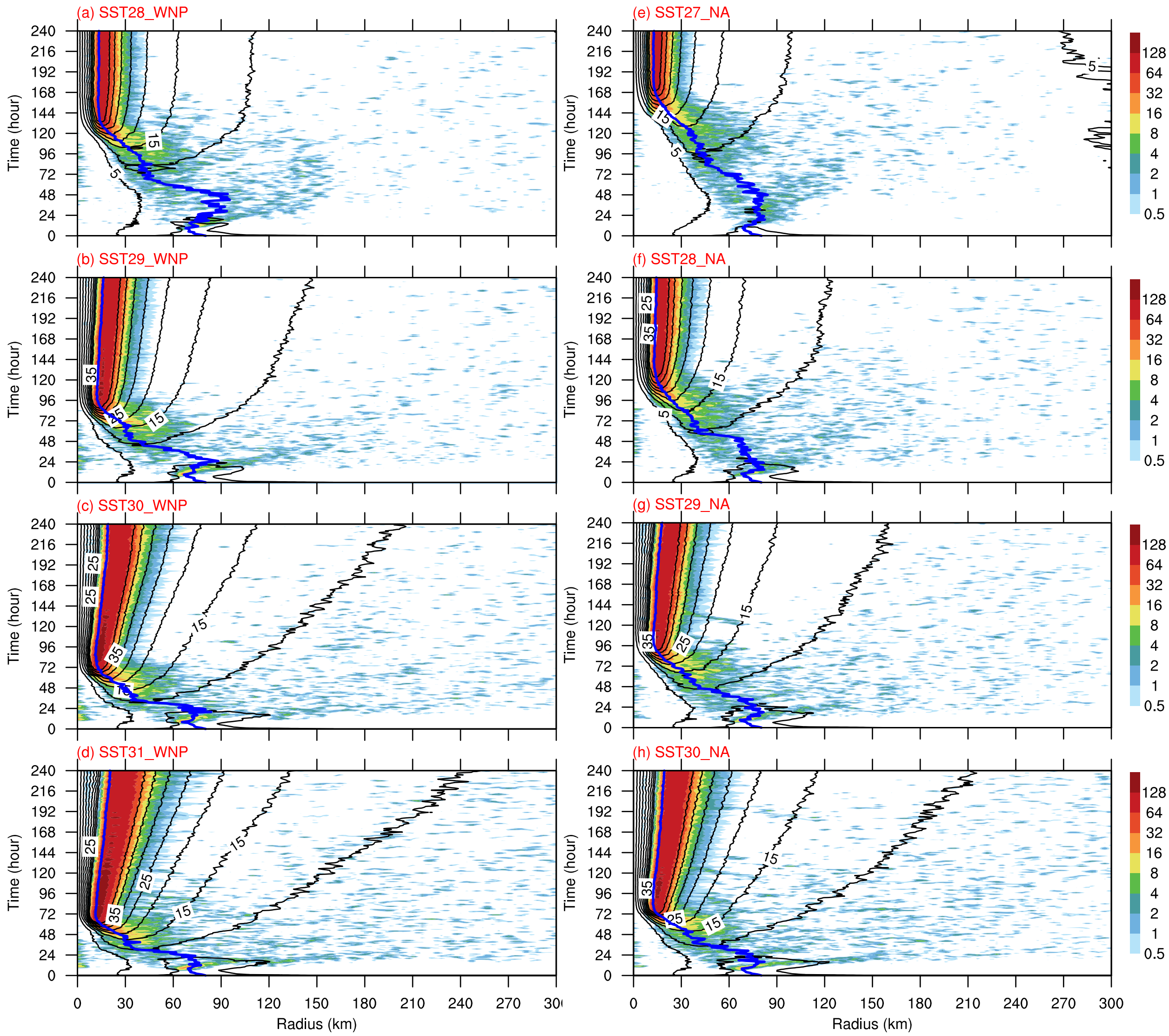

Figure 10. As in Fig. 6 but for results from the experiments using the realistic SST-dependent atmospheric soundings of the WNP (left column) and the NA (right column).

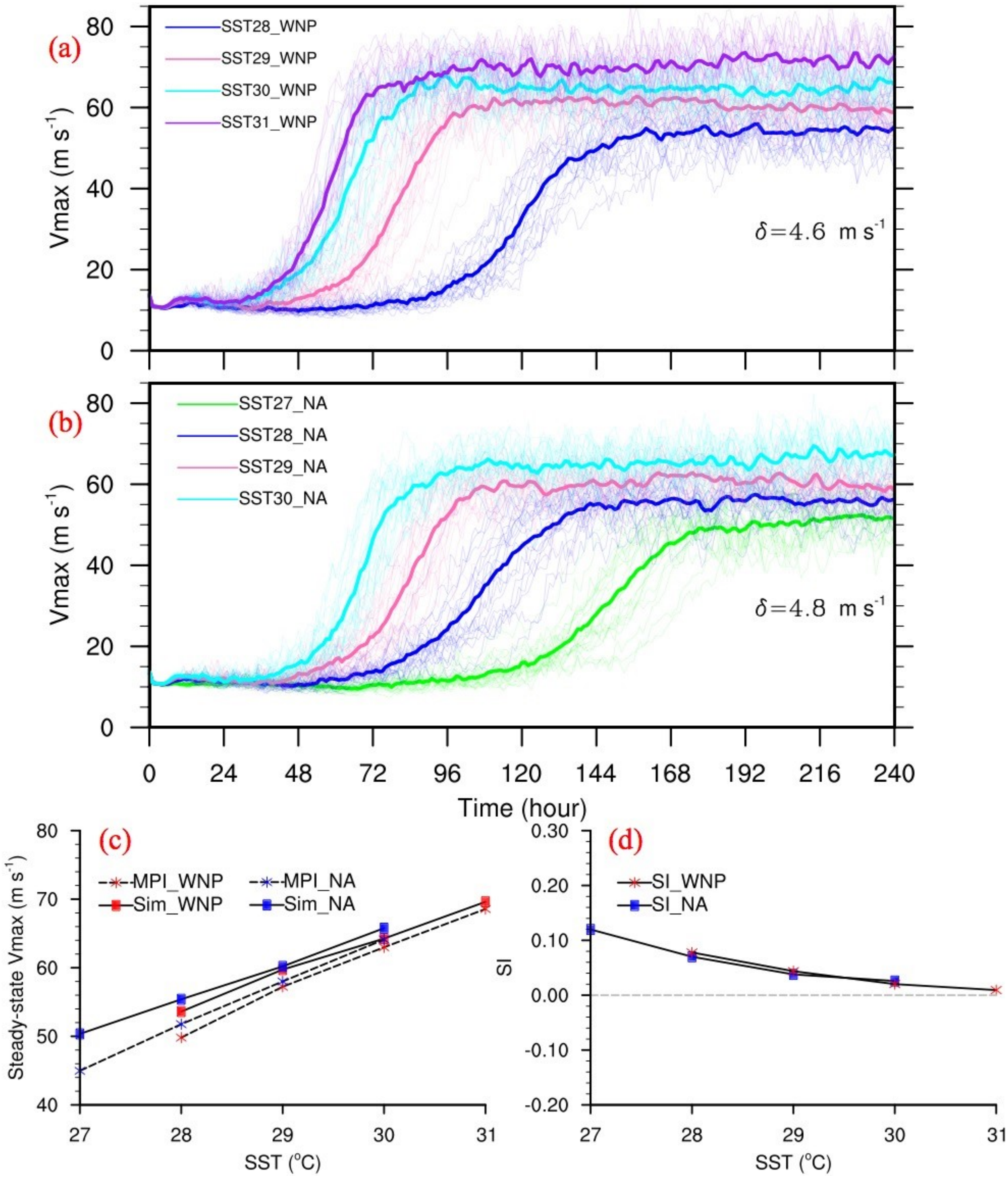

Figure 11. (a)–(b) As in Fig. 1a and (c)–(d) as in Figs. 2a–b, but for results from the experiments using the realistic SST-dependent atmospheric soundings over the WNP and NA, respectively. Sigma value in (a)–(b) indicates the standard deviation for the 21 individual runs averaged among all experiments during 180–240 h.

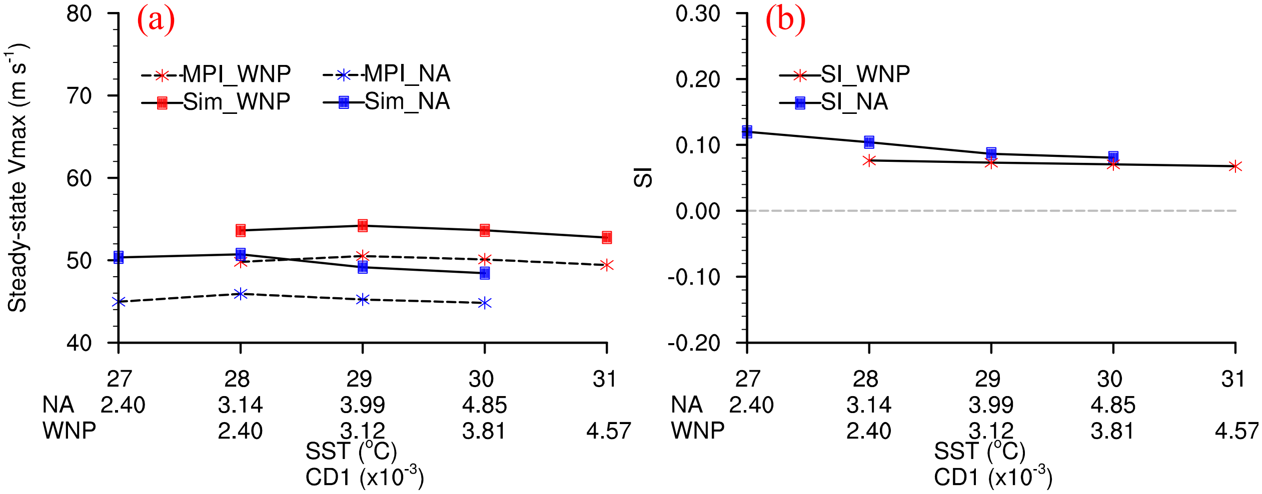

Figure 12. As in Figs. 11c–d, but from the experiments using different upper limit of drag coefficient as shown in the x-axis label.